

Aryl sulfur ligand-modulated silver catalysts with tailored binding affinity for selective nitrate-to-ammonia conversion

Received: 9 September 2025

Accepted: 1 February 2026

Published online: 10 February 2026

Check for updates

Longcheng Zhang^{1,2,6}, Yuan Liu^{2,6}, Ling Li^{3,6}, Xiaoning Li⁴, Pengfei Song², Ting Chen¹, Qian Wu², Justin Zhu Yeow Seow², Kai Tang², Shirong Sun², Xiaodong Guo¹✉ & Zhichuan J. Xu^{2,5}✉

Manipulating the selectivity-determining step in the hydrogenation of nitrogen-containing intermediates is critical to achieving high ammonia selectivity in electrocatalytic nitrate reduction. Here, we propose a molecular interface engineering strategy that functionalized with thiol-anchored aromatic ligands to regulate the interfacial binding affinity and activation of key nitrogen-containing intermediates on silver nanocube surfaces. By systematically varying the electronic properties of the substituents, we identify 4-(methylthio)benzaldehyde as the most effective ligand, increasing the ammonia Faradaic efficiency from 50.8% to 98.9% and achieving a yield rate of 14,366.1 $\mu\text{g h}^{-1} \text{cm}_{\text{geo}}^{-2}$ at -0.63 V versus reversible hydrogen electrode. In situ electrochemical characterizations combined with theoretical simulations further reveal that 4-(methylthio)benzaldehyde modification promotes the activation of weakly hydrogen-bonded water molecules and accelerates the hydrogenation of $^*\text{HNO}$ intermediates. This targeted modulation of interfacial binding affinity offers an effective strategy for selectivity control in electrocatalytic nitrate reduction. The enhanced performance is further validated in a membrane electrode assembly electrolyser, underscoring the practical viability of this molecular design strategy for selective nitrate conversion.

Ammonia (NH_3) is an essential feedstock for nitrogen-based fertilizers, with over 70% used in agriculture and the remainder in industrial sectors, such as polymers, explosives, and synthetic fibers^{1–4}. In 2024, global NH_3 production was approximately 190 million tonnes, with the vast majority synthesized via the centralized, fossil fuel-intensive Haber–Bosch process⁵. This process accounts nearly 1% of global energy use and approximately 1.3% of anthropogenic CO_2 emissions annually, underscoring the urgent need for sustainable and decentralized alternatives⁶. Electrocatalytic nitrate reduction reaction (NO_3RR) has emerged as a promising strategy for low-temperature,

low-pressure NH_3 synthesis, offering the added benefit of remediating nitrate (NO_3^-) pollutants originating from agricultural runoff and industrial waste streams^{7–12}. Nevertheless, the multi-electron nature of this transformation limits the efficiency of NO_3^- -to- NH_3 conversion^{13–15}. Therefore, it is critical to develop highly active electrocatalysts to further promote sustainable NH_3 synthesis.

Silver (Ag) exhibits high activity for NO_3^- activation and enables highly selective conversion of NO_3^- to NO_2^- over a broad potential window^{16–18}. However, its weak binding to nitrogen-containing intermediates hinders further conversion to NH_3 . Among various strategies,

¹School of Chemical Engineering, Sichuan University, Chengdu, China. ²School of Materials Science and Engineering, Nanyang Technological University, Singapore, Singapore. ³Analytical & Testing Center, Sichuan University, Chengdu, China. ⁴Centre for Atomaterials and Nanomanufacturing (CAN), School of Science, RMIT University, Melbourne, VIC, Australia. ⁵Centre for Advanced Catalysis Science and Technology, Nanyang Technological University, Singapore, Singapore. ⁶These authors contributed equally: Longcheng Zhang, Yuan Liu, Ling Li. ✉ e-mail: xiaodong2009@scu.edu.cn; xuzc@ntu.edu.sg

ligand functionalization is attractive owing to its tunability and precise control of local electronic environments. Introducing ligands with tailored electronic or steric properties enables fine-tuning of intermediate binding^{19,20}. For example, pyridine-functionalized Ag electrodes exhibit enhanced NO₃⁻ adsorption in the initial step, leading to a nearly fivefold increase in NH₃ production, highlighting the potential of organic molecules in steering NO₃RR pathways¹⁸. In addition to electronic modulation, maintaining interfacial stability under reductive electrochemical conditions is also critical. Thiol-terminated ligands can form strong coordination bonds with metal surfaces²¹, remaining anchored during operation and thereby preserving catalyst-electrolyte interfacial integrity. Although preliminary studies have demonstrated the role of organic ligands in tuning NO₃RR performance, the mechanistic understanding remains incomplete. Moreover, extending these insights to supported metal nanocatalysts under device-relevant conditions is essential for demonstrating the practical relevance of molecular-level strategies.

Here, we report a surface engineering strategy that employs aryl sulfur ligands to tailor the electronic properties of Ag nanocubes (Ag NCs) for NO₃⁻ electroreduction. Density functional theory (DFT) calculations reveal that aryl sulfur ligands with distinct electronic characteristics modulate the charge distribution of surface Ag atoms, which significantly influences the energy barriers of key reaction steps, including *NO₃ adsorption, *NO₃ dissociation, and H₂O activation. Among the investigated systems, 4-(methylthio)benzaldehyde-functionalized Ag NCs (MTBA-Ag NCs) exhibit more favorable intermediate binding, achieving a high NH₃ yield rate of 14,366.1 μg h⁻¹ cm_{geo}⁻² with a Faradaic efficiency (FE) of 98.9% (compared with 50.8% for unmodified Ag NCs). In situ electrochemical characterizations combined with theoretical simulations further demonstrate that MTBA modification facilitates the activation of weakly hydrogen-bonded H₂O and accelerates the hydrogenation of *HNO intermediates. X-ray absorption spectroscopy (XAS) measurements confirm that MTBA stabilizes the surface oxidation state of Ag under reaction conditions. Importantly, in a membrane electrode assembly (MEA) electrolyzer, MTBA modification markedly enhances NO₃RR activity, validating its practical applicability. A preliminary techno-economic analysis (TEA) highlights the critical role of wastewater-derived NO₃⁻ and low electricity costs (≤ US\$0.04 kWh⁻¹) in enabling sustainable ammonia electro-synthesis.

Results

Aryl sulfur ligand screening on Ag NCs for NO₃⁻ electroreduction

To elucidate the role of surface functionalization in tuning catalytic activity, we functionalized Ag NCs with five representative para-substituted aryl sulfur ligands (Fig. 1a). The sulfur atom anchors to the Ag surface and the para position bears distinct substituents: 4-methylbenzenethiol (p-CH₃, MBT), 4-aminothiophenol (p-NH₂, ATP), 4-mercaptophenol (p-OH, MP), 4-(methylthio)benzaldehyde (p-CHO, MTBA), and 4-mercaptobenzoic acid (p-COOH, MBA). These ligands span from electron-donating to electron-withdrawing substituents, enabling a systematic correlation between ligand electronic character and catalytic performance. To probe the electrocatalytic response, cyclic voltammetry (CV) was performed on pristine and ligand-modified Ag NCs in Ar-saturated 1 M KOH with and without 2,000 ppm NO₃⁻. As shown in Fig. 1b, both Ag NCs and MTBA-Ag NCs exhibit two well-defined reduction regions, corresponding to the stepwise reduction of NO₃⁻ (region 1) and NO₂⁻ (region 2) in Ar-saturated 1 M KOH containing 2000 ppm NO₃⁻²². Notably, the MTBA-Ag NCs demonstrate substantially highest current densities in both regions, indicative of enhanced catalytic activity for NO₃⁻ reduction (Supplementary Figs. 1–3). Furthermore, the NO₂⁻ reduction peak (region 2) is shifted to more positive potentials for MTBA-Ag NCs, suggesting a lower energy barrier resulting from surface modification by MTBA^{17,23}.

To screen aryl sulfur ligands on Ag NCs, DFT calculations were carried out on an ideal Ag (100) slab²⁴. We first quantified the electronic character of the para-substituted aryl sulfur ligands by Bader charge analysis (Fig. 1c and Supplementary Table 1), as these substituents capture the intrinsic electronic effects while avoiding steric interference²⁵. The p-CH₃ group carries a negative Bader charge (−0.21 e⁻), consistent with electron donation that increases interfacial electron density and lowers the calculated valence of neighboring Ag atoms. In contrast, increasingly electron-withdrawing substituents, namely p-NH₂ (0.36 e⁻), p-OH (0.51 e⁻), p-CHO (1.03 e⁻), and p-COOH (2.16 e⁻), exhibit progressively positive charges, indicating net electron withdrawal from the Ag surface and a concomitant increase in the valence of surface Ag atoms. These results establish a clear correlation between substituent electronics, interfacial charge transfer, and Ag valence. We next examined how this charge transfer manifests spatially. Mapping the oxidation states of Ag atoms adjacent to grafting sites shows that MTBA functionalization produces a pronounced increase in the valence of neighboring Ag atoms (Fig. 1d and Supplementary Fig. 4). Structural optimizations further show that none of the aryl sulfur ligands introduce significant steric crowding, aromatic-ring distortion or blockage of adjacent adsorption sites. ATP-Ag NCs, MP-Ag NCs, and MBA-Ag NCs display similar enhancements to varying extents, correlating with the electron-withdrawing strength of the substituent (Supplementary Table 2). In contrast, MBT functionalization lowers the valence of surface Ag atoms. Thus, the intrinsic electronic character of the substituent, together with its interfacial interactions, determines the oxidation states of surface Ag atoms.

As NO₃⁻ reduction generally commences with *NO₃ chemisorption²⁶, we then assessed how the ligands tune both associative adsorption and dissociative activation on Ag (100) (Fig. 1e and Supplementary Figs. 5–7). Associative adsorption is strong on Ag NCs (−1.67 eV) and MP-Ag NCs (−1.59 eV), consistent with the Sabatier principle, which can impede catalytic turnover²⁷. The *NO₃ → *NO₂ step is endothermic on all surfaces. ATP-Ag NCs and MTBA-Ag NCs incur the two lowest penalties (0.11 and 0.17 eV, respectively), which are lower than those on MBT-Ag NCs (0.25 eV) and MBA-Ag NCs (0.22 eV), indicating more facile dissociation on the former surfaces. Moreover, the ATP-Ag NCs and MTBA-Ag NCs exhibit notably lower kinetic barriers compared to the other catalysts, indicating more favorable kinetics toward NO₃⁻ reduction (Supplementary Fig. 8). On this basis, ATP-Ag NCs and MTBA-Ag NCs were shortlisted for further study. In addition, because hydrogen is supplied by H₂O dissociation during NO₃⁻-to-NH₃ conversion²⁸, we further assessed H₂O adsorption and found that ATP-Ag NCs disfavor H₂O dissociation (+0.70 eV). Considering adequate *NO₃ adsorption, facile dissociation, and favorable H₂O adsorption, MTBA-Ag NCs emerge as the most promising candidate. Under Ar and potential-step operation, online differential electrochemical mass spectrometry (DEMS) reveals well-defined, potential-dependent responses at *m/z* = 17, 30, 31, and 33, assigned to NH₃, NO, NOH/HNO, and NH₂OH, whereas the signals at *m/z* = 28 and 46 (N₂ and NO₂) remain close to the baseline (Fig. 1f). These features indicate a dominant single-nitrogen pathway in which *NO₃ is stepwise deoxygenated via a short-lived *NO₂ intermediate to *NO and *NOH, followed by further hydrogenation to highly reduced *NH_x species and NH₃. Free-energy profiles clarify the thermodynamic landscape of this pathway (Fig. 1g; Supplementary Tables 3 and 4), and the optimized adsorption geometries are shown in Supplementary Figs. 9 and 10. Among all elementary steps, the *NO₂-to-*NO hydrogenation exhibits the largest free-energy barrier and therefore defines the rate-determining step (RDS) on both MTBA-Ag NCs and Ag NCs. The corresponding barrier is 1.18 eV on MTBA-Ag NCs, slightly lower than 1.22 eV on Ag NCs, indicating that the MTBA ligand environment favorably modulates the *NO₂-to-*NO conversion barrier. To validate the robustness of this mechanistic insight, we additionally evaluated the *NO₂ → *NO step using an implicit solvation model combined with a constant-potential approach spanning −0.4 to 0.4 V versus RHE. Across

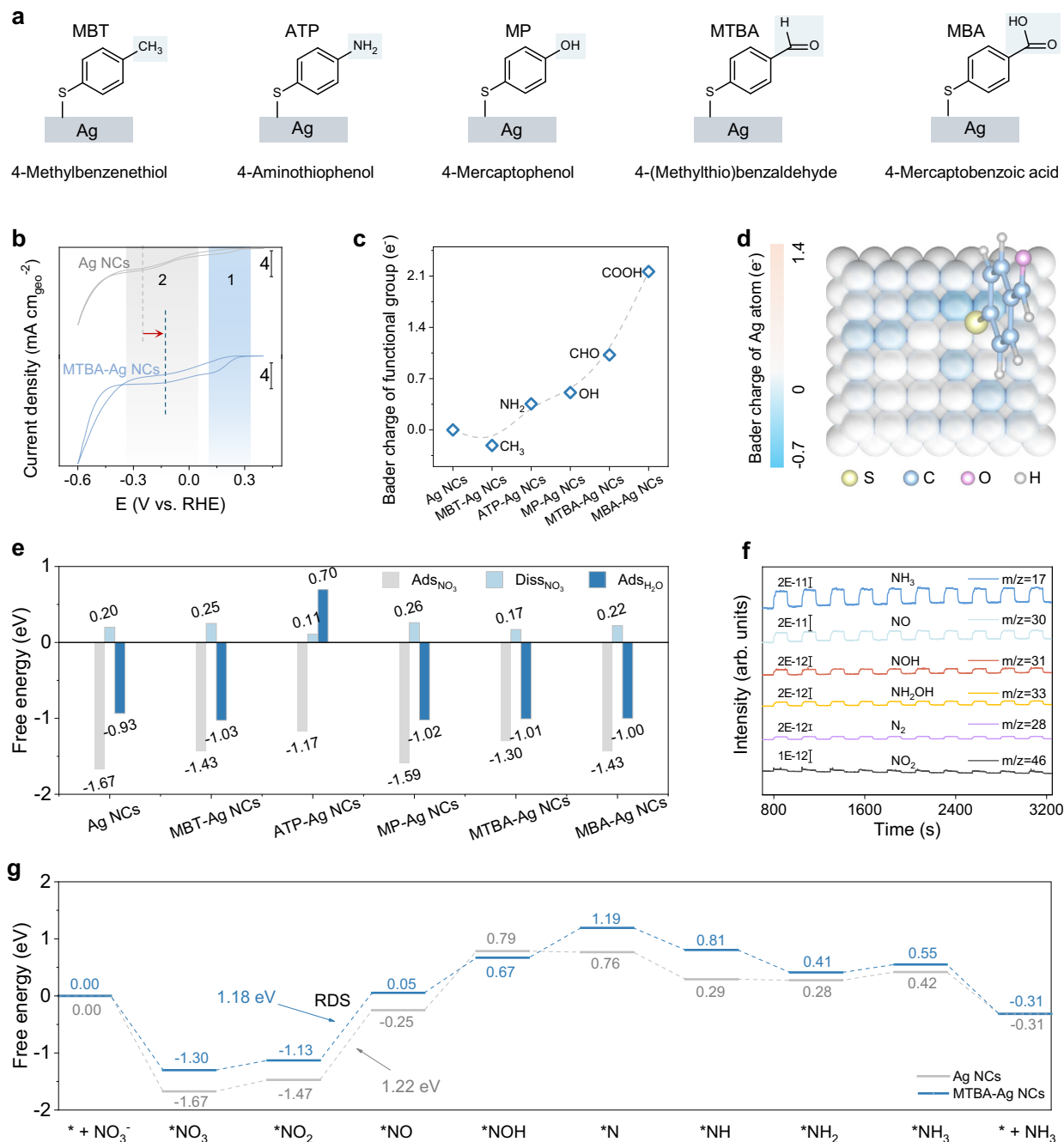


Fig. 1 | Rational Ligand Screening on Ag NCs for NO_3RR . **a** Chemical structure of para-substituted aryl sulfur ligands used to functionalize Ag NCs: MBT, ATP, MP, MTBA, and MBA. **b** Cyclic voltammograms of Ag NCs and MTBA-Ag NCs in Ar-saturated 1 M KOH containing 2,000 ppm NO_3^- , measured at a scan rate of 50 mV s^{-1} . **c** Bader charge of the para substituents adsorbed on an Ag (100) slab. **d** Heat map of Bader charge on Ag (100) surface atoms following MTBA grafting.

Ag atoms are colored by their Bader charges from -0.7 (blue) to 1.4 (orange). **e** Calculated free energies for $^*\text{NO}_3$ adsorption (Ads_{NO_3}), $^*\text{NO}_3$ dissociation to $^*\text{NO}_2$ ($\text{Diss}_{\text{NO}_3}$), and H_2O adsorption ($\text{Ads}_{\text{H}_2\text{O}}$) on Ag NCs and aryl sulfur-ligand-modified Ag NCs. **f** Electrochemical online DEMS results for the NO_3RR over MTBA-Ag NCs. **g** Reaction free-energy profiles for conversion of NO_3^- to NH_3 on Ag NCs and MTBA-Ag NCs.

this potential window, the RDS barrier on Ag NCs remains consistently higher than that on MTBA-Ag NCs (Supplementary Fig. 11), confirming that the MTBA-induced enhancement in NO_3RR activity persists even when solvation and electrode-potential effects are explicitly included.

Characterization of aryl sulfur ligand-functionalized Ag NCs

Inspired by the theoretical insights, we fabricated a series of aryl sulfur-modified Ag NCs. Specifically, the aryl sulfur-modified Ag NCs were synthesized via a modified polyol process using silver nitrate and trace

copper (II) chloride as precursors, followed by post-synthetic surface modification with aryl sulfur ligands in ethanol/isopropanol solution^{29,30}. Powder X-ray diffraction (XRD) analysis confirms that ligand functionalisation does not alter the crystalline structure of the Ag NCs (Fig. 2a). The diffraction patterns of Ag NCs and aryl sulfur-modified Ag NCs are nearly identical, showing the characteristic peaks of face-centered cubic metallic silver (JCPDS No. 04-0783). Scanning electron microscopy (SEM) and transmission electron microscopy (TEM) further reveal that the cubic morphology and size of the Ag NCs

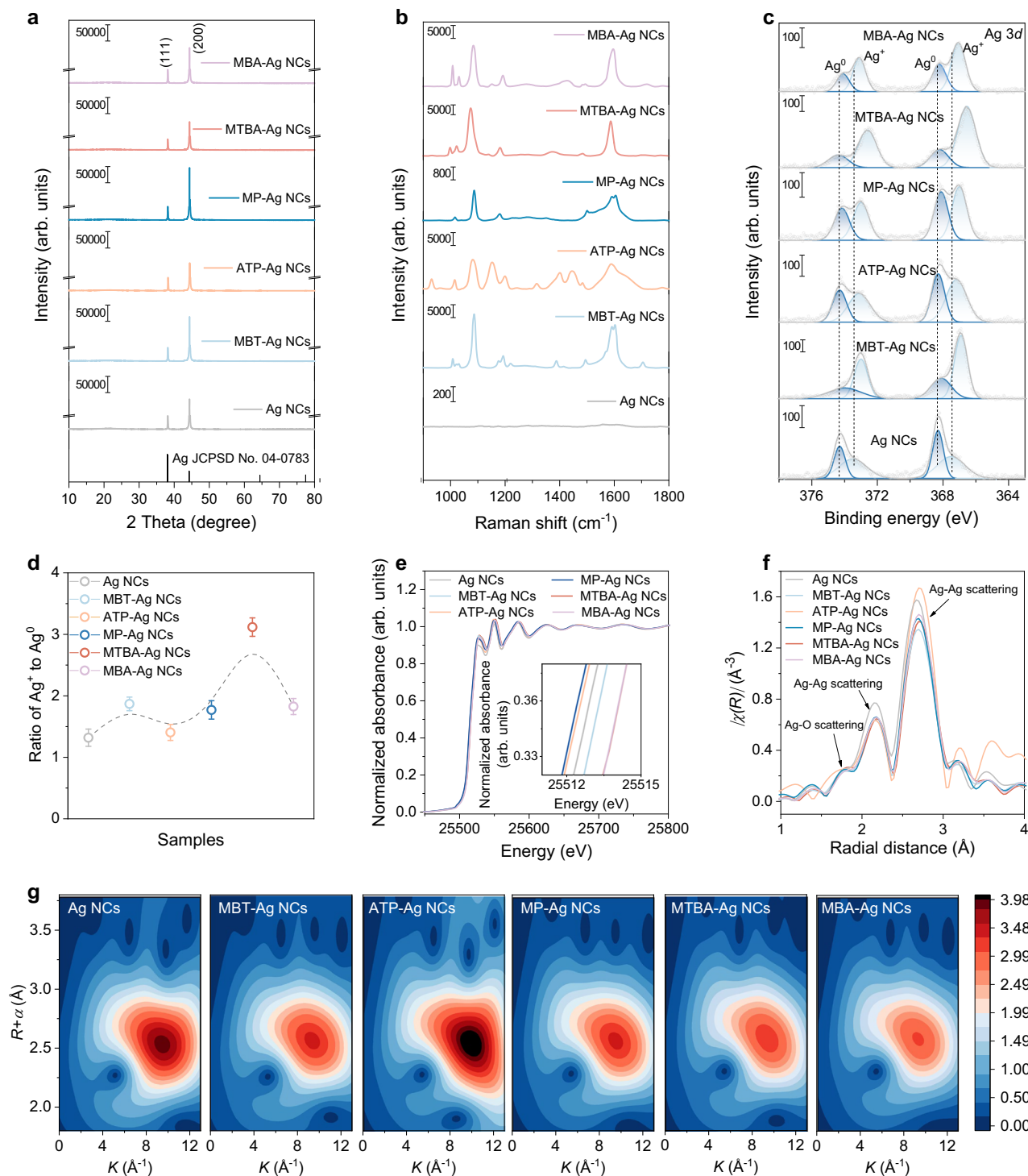


Fig. 2 | Structural characterization of Ag NCs and aryl sulfur-modified Ag NCs. **a** XRD patterns, **b** Raman spectra, and **c** high-resolution Ag 3d XPS spectra of Ag NCs and aryl sulfur-modified Ag NCs. **d** Ratio of Ag⁺ to Ag⁰ in Ag NCs and aryl sulfur-modified Ag NCs derived from high-resolution Ag 3d XPS spectra. The analysis was

performed at least three times, and the mean values are shown with the standard deviation as error bars. **e** Ag K-edge XANES, **f** Fourier transform of Ag K-edge EXAFS spectra, and **g** WT-EXAFS plots of Ag NCs and aryl sulfur-modified Ag NCs.

remain unchanged after ligand functionalization (Supplementary Figs. 12 and 13). The consistent shape and dimensions indicate that the structural and morphological stability of the nanocubes is preserved during the modification process, with no observable aggregation or deformation. Energy-dispersive X-ray spectroscopy elemental mapping shows uniform distributions of Ag, S, N, and O on ATP-Ag NCs, indicating the successful introduction of nitrogen-containing functional groups. By contrast, MBT-, MP-, MTBA-, and MBA-Ag NCs display

homogeneous distributions of Ag, S, and O, consistent with the elemental composition of their respective ligands (Supplementary Fig. 14). Supplementary Fig. 15 shows high-angle annular dark-field scanning TEM (HAADF-STEM) images of Ag NCs functionalized with the different ligands. Clear lattice fringes are observed, with interplanar spacings ranging from 0.20 to 0.23 nm, which vary slightly with ligand identity (Supplementary Table 5). These variations indicate that the surface ligands induce subtle yet measurable changes in the Ag

lattice structure, likely arising from differences in ligand-metal interactions.

Raman spectroscopy confirms the successful surface functionalization of Ag NCs with the substituted aryl sulfur ligands. As shown in Fig. 2b, the Ag NCs exhibit no discernible Raman signals in the measured range (900–1800 cm^{-1}), indicating an absence of molecular vibrations. By contrast, all aryl sulfur-modified Ag NCs display well-defined and ligand-specific Raman peaks, demonstrating effective ligand attachment. Detailed peak assignments are summarized in Supplementary Table 6. Together, these results confirm that the aryl sulfur ligands are anchored on the Ag NC surfaces and retain their chemical identity, enabling molecularly defined surface modification. X-ray photoelectron spectroscopy (XPS) reveals that the substituted aryl sulfur ligands significantly modulate the surface chemical state of Ag NCs. As shown in Fig. 2c, Ag NCs show dominant Ag^0 signals at 368.3 eV and 374.3 eV, corresponding to the $\text{Ag } 3d_{5/2}$ and $3d_{3/2}$, respectively. Additional peaks at -367.5 eV and -373.4 eV are assigned to Ag^+ species, likely arising from surface oxidation^{31,32}. Upon ligand modification, the Ag^+ peaks in all samples shift to lower binding energies, suggesting that ligand coordination perturbs the local electronic environment and promotes a higher apparent oxidation state of surface Ag atoms. Notably, the Ag^+/Ag^0 ratio increases in all ligand-protected NCs relative to Ag NCs (Fig. 2d), with MTBA-Ag NCs exhibiting the largest Ag^+ fraction. This trend correlates with the electron-withdrawing character of the substituents, which stabilize oxidized Ag species and induce chemical shifts by modulating the surface charge density. XAS reveals that substituted aryl sulfur ligands modulate the local structure and electronic state of Ag NCs. As shown in Fig. 2e, the Ag K-edge X-ray absorption near edge structure (XANES) of the ligand-modified Ag NCs shifts in a ligand-dependent manner relative to Ag NCs. Several samples exhibit positive edge shifts, consistent with electron transfer from Ag to electron-withdrawing ligands and an increase in the average Ag valence. In contrast, ATP-Ag NCs and MP-Ag NCs display slight negative shifts, indicating net electron donation to the Ag core and a lower average Ag valence. Among the positively shifted samples, MTBA-Ag NCs show the largest upshift, suggesting the strongest oxidation effect. This trend mirrors the Ag 3 *d* XPS results and further supports the presence of oxidized Ag species at the Ag NCs surface. The Fourier-transformed k^2 -weighted extended X-ray absorption fine structure (EXAFS) (Fig. 2f) reveals three prominent features at -1.75 Å, -2.17 Å, and -2.70 Å, attributable to Ag–O coordination and to the first and second Ag–Ag shells, respectively^{33–36}. To quantify these observations, Ag K-edge EXAFS fitting was performed for Ag foil, Ag NCs, and all ligand-modified samples (Supplementary Figs. 16, 17, and Supplementary Table 7). The fits reveal that the first-shell Ag–Ag coordination is largely preserved across all samples, with nearly identical bond distances and low Debye-Waller factors, indicating that the Ag core lattice remains essentially intact upon ligand coordination. In contrast, the Ag–O shell exhibits ligand-dependent variations in coordination number and bond distance, reflecting differences in the extent and mode of ligand coordination at the surface. Notably, MTBA-Ag NCs exhibit a substantially amplified Ag–O contribution, reflecting stronger Ag–ligand coordination at the expense of metallic connectivity. Such variations in local structure point to ligand-dependent restructuring of the Ag surface, which is likely to influence both the electronic structure and the catalytic properties of the nanocubes³⁴. Wavelet-transform (WT) analysis of the Ag K-edge EXAFS (Fig. 2g) reveals a dominant intensity maximum at $-9\text{--}10 \text{ \AA}^{-1}$ ($R + \alpha \approx 2.5\text{--}2.7 \text{ \AA}$), characteristic of first-shell Ag–Ag coordination. The Ag–Ag feature is ligand-dependent: ATP-Ag NCs show the most pronounced maximum, whereas MTBA-Ag and MBA-Ag NCs display attenuated intensities relative to Ag NCs, with MBT-Ag NCs and MP-Ag NCs remaining comparable. A low- k feature ($-4\text{--}6 \text{ \AA}^{-1}$, $R + \alpha \approx 1.7\text{--}2.0 \text{ \AA}$), attributable to Ag–O scattering, is at best weak in these maps, precluding firm trend assignments from WT alone^{37–39}.

NO₃RR performance

The NO₃RR performance of Ag NCs and five aryl sulfur-modified Ag NCs catalysts was evaluated by linear sweep voltammetry (LSV), with Ag NCs as the control (Fig. 3a and Supplementary Fig. 18). LSV curves of Ag NCs, MBT-Ag NCs, ATP-Ag NCs, MP-Ag NCs, MTBA-Ag NCs, and MBA-Ag NCs in Ar-saturated 1 M KOH containing 2000 ppm NO_3^- revealed that MTBA-Ag NCs delivered the highest cathodic current density for NO_3^- reduction, followed by ATP-Ag NCs and MP-Ag NCs. Furthermore, as shown in Fig. 3b, MTBA-Ag NCs consistently achieved the lowest potentials to reach current densities of 50, 100, and 200 mA cm^{-2} , indicating enhanced electrocatalytic activity toward NO₃RR. In contrast, MBT-functionalized Ag NCs required higher potentials than Ag NCs at all evaluated current densities, indicating a suppression of NO₃RR activity. In this study, concentrations of NH_3 , NO_2^- , and residual NO_3^- were quantified by ultraviolet-visible (UV-Vis) spectrophotometry (Supplementary Figs. 19–21). Figure 3c presents the NH_3 FEs over Ag NCs and aryl sulfur-modified Ag NCs catalysts in 1 M KOH containing 2,000 ppm NO_3^- . MTBA-Ag NCs consistently showed higher NH_3 FEs across the potential range than Ag NCs, reaching a maximum FE of 98.9% at -0.63 V vs. the reversible hydrogen electrode (RHE), higher than Ag NCs (50.8%). At this potential, the corresponding H_2 FE on MTBA-Ag NCs was only 0.9% (Supplementary Fig. 22). Notably, MP-Ag NCs and ATP-Ag NCs displayed lower NH_3 FEs than Ag NCs between -0.47 V and -0.63 V vs. RHE, likely due to the competing hydrogen evolution reaction (HER) that diminishes NO_3^- reduction (Supplementary Figs. 23 and 24). Figure 3d compares the NH_3 yield rates and energy efficiencies (EE) of Ag NCs and five aryl sulfur-modified Ag NCs catalysts. The unmodified Ag NCs delivered a peak NH_3 yield rate of $5798.9 \mu\text{g h}^{-1} \text{ cm}_{\text{geo}}^{-2}$ at -0.70 V vs. RHE, with an EE of 14.6%. Functionalization with aryl sulfur ligands generally led to improved performance. MTBA-Ag NCs achieved the highest yield rate of $14,366.1 \mu\text{g h}^{-1} \text{ cm}_{\text{geo}}^{-2}$ and an EE of 33.4%, representing a 2.5-fold increase in NH_3 production relative to Ag NCs. Notably, MBA-Ag NCs showed a lower NH_3 yield rates than unmodified Ag NCs under identical conditions. These results demonstrate the pronounced impact of surface functionalization on NO₃RR activity and efficiency. To exclude any possible influence of residual Cu introduced by the CuCl_2 -assisted polyol synthesis, we quantified both bulk and surface Cu contents and benchmarked a Cu-free Ag control, all of which confirmed that Cu is below detection and that the activity trends are retained (Supplementary Figs. 25–27). Importantly, macroscopic wettability was essentially the same across all samples (static water contact angles of $115\text{--}125^\circ$; Supplementary Fig. 28), ruling out wetting-induced mass-transport effects as the origin of the observed trends.

Figure 3e shows the partial current densities for NH_3 production as a function of applied potential for Ag NCs and a series of aryl sulfur-modified Ag NCs. All catalysts exhibited increasing partial current density at more negative potentials, although the magnitude of enhancement varied substantially. MTBA-Ag NCs showed the largest partial current density of $-187.4 \text{ mA cm}^{-2}$ at -0.71 V vs. RHE. ATP-Ag NCs also exhibited appreciable activity, showing improved performance metrics compared with Ag NCs and other aryl sulfur-modified Ag NCs, including MBT-Ag NCs, MP-Ag NCs, and MBA-Ag NCs. For MTBA-Ag NCs, partial-current analysis further shows that the current associated with NH_3 formation almost coincides with the total cathodic current, whereas the summed partial current for all other products, including H_2 , remains very small (Supplementary Fig. 29), underscoring its near-unity NH_3 selectivity and strongly suppressed HER. Supplementary Fig. 30 compares the NH_3 yield rates and FEs of recently reported NO₃RR catalysts. At low-concentration NO_3^- conditions, the MTBA-Ag NCs in this work exhibited a clear performance advantage, achieving a high NH_3 yield rate of $14,366.1 \mu\text{g h}^{-1} \text{ cm}_{\text{geo}}^{-2}$ with a FE approaching 98.9%. These metrics are compared with representative reported systems in Supplementary Table 8.

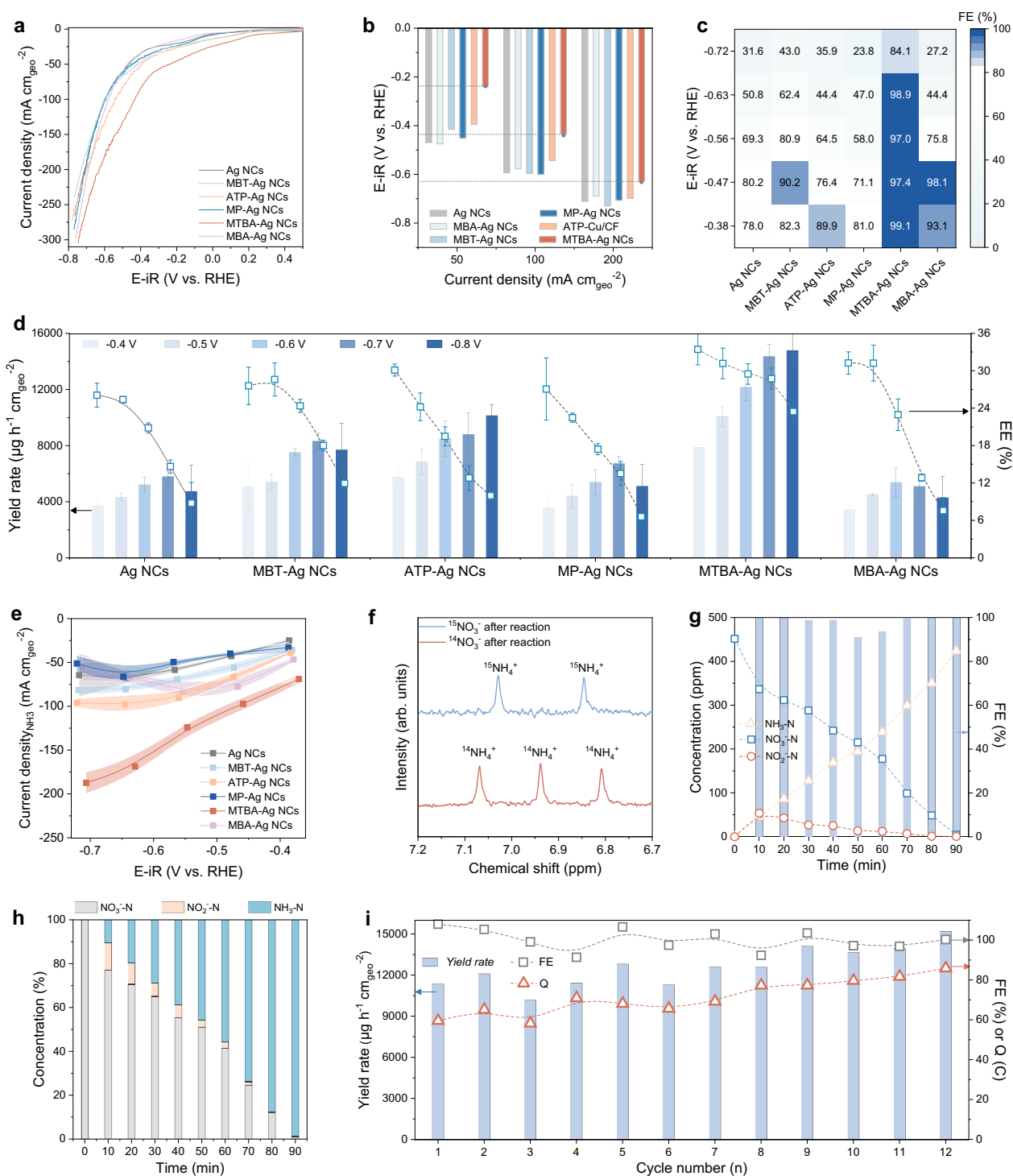


Fig. 3 | NO₃RR performance of Ag NCs and aryl sulfur-modified Ag NCs.

a Polarization curves, **b** potentials comparison, **c** FEs, **d** yield rates and EE, and **e** partial current densities of NH₃ for Ag NCs and aryl sulfur-modified Ag NCs. Data represent mean values with standard deviation error bars ($n \geq 3$). **f** ¹H NMR spectra of products using K¹⁵NO₃ or K¹⁴NO₃. **g** Time-dependent concentrations of NO₃⁻-N,

NO₂⁻-N, and NH₃-N, and the corresponding NH₃ FE over MTBA-Ag NCs. **h** Product ratios as a function of time during complete NO₃⁻ conversion over MTBA-Ag NCs. **i** NH₃ yield rates, FEs, and Q of MTBA-Ag NCs over 12 consecutive cycles. All measurements were conducted in Ar-saturated 1M KOH containing 2000 ppm NO₃⁻.

To verify the origin of nitrogen in the generated NH₃, isotope-labeling experiments were performed using ¹⁵NO₃⁻ as the nitrogen source. The resulting ¹H nuclear magnetic resonance (NMR) spectra (Fig. 3f) exhibited a distinct doublet diagnostic of ¹⁵NH₄⁺, in clear contrast to the triplet for ¹⁴NH₄⁺, thereby enabling precise isotopic differentiation. The exclusive detection of ¹⁵NH₄⁺ in the ¹⁵NO₃⁻ system

confirms that NH₃ originated from the electroreduction of NO₃⁻ in the electrolyte, effectively excluding adventitious nitrogen sources. Moreover, the NH₃ yield rates determined by ¹H NMR agreed well with those obtained via UV-Vis spectroscopy (Supplementary Fig. 31), reinforcing the reliability and robustness of the NMR-based quantification method.

To evaluate the practical applicability, we assessed its NO_3^- removal performance in a simulated wastewater (2,000 ppm NO_3^-) using MTBA-Ag NCs. As illustrated in Fig. 3g, the concentration of NO_3^- -N decreased steadily over time, accompanied by a concomitant increase in NH_3 -N concentration, indicating efficient conversion of NO_3^- to NH_3 . Importantly, the intermediate NO_2^- -N remained at negligible levels throughout the process, suggesting a direct and selective pathway for NO_3^- reduction (Fig. 3h). Notably, both NO_3^- and NO_2^- concentrations were reduced below the World Health Organization drinking-water guideline limits within 90 min⁴⁰, while the FE for NH_3 consistently exceeded 90%. This rapid and efficient NO_3^- reduction underscores the potential of MTBA-Ag NCs for practical wastewater-treatment applications.

The long-term operational stability of MTBA-Ag NCs for NO_3RR was assessed via repeated electrolysis cycles. As shown in Fig. 3i and Supplementary Table 9, the NH_3 yield rate, FE and total charge (Q) remained essentially constant over 12 consecutive cycles, indicating negligible degradation. This robust cycling stability highlights the durability of MTBA-Ag NCs under continuous electrochemical operation. Complementary structural and compositional analyses, including XRD, high-resolution XPS, and HADDF-STEM (Supplementary Figs. 32–34), further confirmed preservation of catalyst integrity, underscoring its potential for sustained use in practical NO_3^- remediation.

Mechanistic studies

The activation of H_2O is a critical step in NO_3RR , as it provides the hydrogen required for subsequent hydrogenation step²⁸. Recent advances in Raman spectroscopy enable direct probing of interfacial H_2O structure, particularly the hydrogen-bonding environment at catalyst surfaces^{41,42}. In the O–H stretching region (3000–3800 cm^{-1}), both bare and aryl sulfur-modified Ag NCs exhibited three distinct bands at ~3200, ~3400, and ~3600 cm^{-1} , corresponding to tetrahedrally hydrogen-bonded (4-HB), bidentate (2-HB), and weakly hydrogen-bonded (weak-HB) H_2O species, respectively (Fig. 4a, b and Supplementary Fig. 35)⁴¹. The relative band intensities report on hydrogen-bond strength and, by extension, the propensity of interfacial H_2O to dissociation, with the energetic order weak-HB < 2-HB < 4-HB. Thus, weakly hydrogen-bonded H_2O is more readily cleaved to form adsorbed hydrogen (*H), thereby facilitating hydrogenation steps essential to NO_3RR ⁴³. Upon increasing cathodic bias, the fraction of weak-HB H_2O increased markedly on MTBA-Ag NCs relative to Ag NCs, accompanied by a pronounced red shift of the weak-HB band that reflects strengthened H_2O –catalyst interactions. The extracted Stark tuning rate was 12.55 $\text{cm}^{-1} \text{V}^{-1}$, far exceeding that of Ag NCs (1.54 $\text{cm}^{-1} \text{V}^{-1}$; Fig. 4c), underscoring the enhanced capacity of MTBA-Ag NCs to activate interfacial H_2O ⁴³.

To further evaluate the generation and consumption of hydrogen radicals ($\text{H}\cdot$) during NO_3RR on MTBA-Ag NCs and Ag NCs, quasi in situ electron paramagnetic resonance (EPR) spectroscopy was performed using 5,5-dimethyl-1-pyrroline N-oxide (DMPO) as a spin-trapping agent (Fig. 4d). Following electrolysis in Ar-saturated 1M KOH, a pronounced DMPO-H signal was observed for MTBA-Ag NCs, whereas no detectable signal was observed for Ag NCs, consistent with more efficient H_2O dissociation and $\text{H}\cdot$ generation on the ligand-modified surface. Remarkably, when electrolysis was carried out in Ar-saturated 1M KOH containing 2,000 ppm NO_3^- , the DMPO-H signal on MTBA-Ag NCs was nearly completely quenched, suggesting rapid consumption of $\text{H}\cdot$ during the hydrogenation steps of NO_3RR . These results indicate efficient coupling between H_2O activation and subsequent hydrogenation steps on MTBA-Ag NCs, a key requirement for selective NH_3 formation⁸.

To further gain mechanistic insights into the NO_3RR , in situ Raman spectroscopy was used to track the potential-dependent evolution of surface-bound intermediates on Ag NCs and MTBA-Ag NCs.

As shown in Supplementary Fig. 36, both catalysts exhibited characteristic Raman bands at 912 and 1066 cm^{-1} at open circuit potential, corresponding to the symmetric stretch of the $\delta_{\text{C-S-H}}$ and adsorbed NO_3^- bending mode, respectively⁴⁴. A low-frequency band at 531 cm^{-1} , more pronounced on MTBA-Ag NCs, was assigned to Ag–N stretching, indicating stronger interactions with the MTBA-modified Ag surface⁴⁵. Beyond these shared features, MTBA-Ag NCs displayed additional vibrational signatures at 1183, 1379, 1438, and 1585 cm^{-1} , assigned to C=O stretching modes of surface-bound –CHO groups⁴³. These aldehyde-related modes gradually attenuate at more negative potentials, which we ascribe to potential-dependent interfacial field/orientation effects rather than loss of the MTBA adlayer (Supplementary Figs. 37, 38)⁴⁶. Under applied cathodic potentials ranging from 0.4 to –0.8 V vs. RHE (Fig. 4e, f), the 1066 cm^{-1} band diminished more rapidly on MTBA-Ag NCs than on Ag NCs, suggesting faster consumption or conversion of adsorbed NO_3^- ^{8,47}. Concurrently, a new band at 1543 cm^{-1} emerged, assigned to the N–O stretch of adsorbed HNO⁴⁸. This feature appeared at considerably more positive potentials on MTBA-Ag NCs (as early as –0.1 V vs. RHE), whereas on Ag NCs it did not appear until –0.3 V and with substantially lower intensity. The earlier onset and stronger intensity of the *HNO band on MTBA-Ag NCs demonstrate that *H–N coupling is kinetically promoted at the ligand-modified interface. Taken together with the H_2O -activation trends and EPR results, a simple Langmuir-Hinshelwood microkinetic analysis (Supplementary Note 1) indicates that the available *H is kinetically channeled into NO_x hydrogenation pathways rather than H_2 evolution. Using adsorbed * H_2O as the reference ($G = 0.00 \text{ eV}$), H_2O dissociation is an endothermic reaction on Ag NCs ($\Delta G = +0.86 \text{ eV}$) but exothermic on MTBA-Ag NCs ($\Delta G = -0.63 \text{ eV}$) (Fig. 4g and Supplementary Table 10). The favourable thermodynamics on the MTBA-modified surface indicate a lower energetic barrier for H_2O dissociation, consistent with the larger Stark tuning rate and the EPR evidence of enhanced $\text{H}\cdot$ formation. In the Fourier-transformed EXAFS spectra (Fig. 4h), the Ag–O coordination peak of MTBA-Ag NCs remained clearly visible after NO_3RR , while the Ag–Ag features showed negligible change. To quantitatively assess this stability, post-reaction EXAFS fitting shows that the Ag–Ag coordination shell retains nearly unchanged bond distance and coordination number within experimental uncertainty, with only a slight increase in the Debye-Waller factor (Supplementary Fig. 39 and Table 11). The weak intensity variation at low R for Ag–O is attributed to surface adsorption or hydration, a common effect for noble-metal surfaces under alkaline electrochemical environments^{49–51}. The retention of Ag–O interactions under reaction conditions suggests that oxygenated species remain stably anchored at the catalyst surface (Supplementary Fig. 40). These Ag–O moieties may act as interfacial reservoirs that stabilize *H via hydrogen bonding or weak adsorption, thereby positioning reactive hydrogen near nitrogenous intermediates. Figure 4i summarizes the proposed NO_3RR pathways on Ag NCs and MTBA-Ag NCs surfaces. On Ag NCs, weak Ag– H_2O interactions hinder H_2O dissociation, resulting in a distant hydrogen-bonded network and insufficient local *H, which slows * NO_2 hydrogenation. In contrast, MTBA-Ag NCs introduce Ag^{δ+} sites that facilitate interfacial H_2O activation and generate proximal *H, which couples efficiently with * NO_2 and *HNO to accelerate hydrogenation steps and enhance NH_3 formation. This spatial coupling is consistent with the stronger *HNO Raman signals observed, providing a mechanistic rationale for the improved NO_3RR activity.

Potential industrial application

To assess the industrial feasibility of NO_3RR under ambient conditions, a MEA electrolyzer was constructed using MTBA-Ag NCs on carbon paper (MTBA-Ag NCs/CP; $1.5 \times 1.5 \text{ cm}^2$) as the cathode and NiFe-LDHs on nickel foam (NiFe-LDHs/NF; $1.5 \times 1.5 \text{ cm}^2$) as the anode (Supplementary Fig. 41). The MTBA-Ag NCs/CP-based MEA exhibited lower impedance and delivered approximately 232 mA cm^{-2} at 2.0 V, over

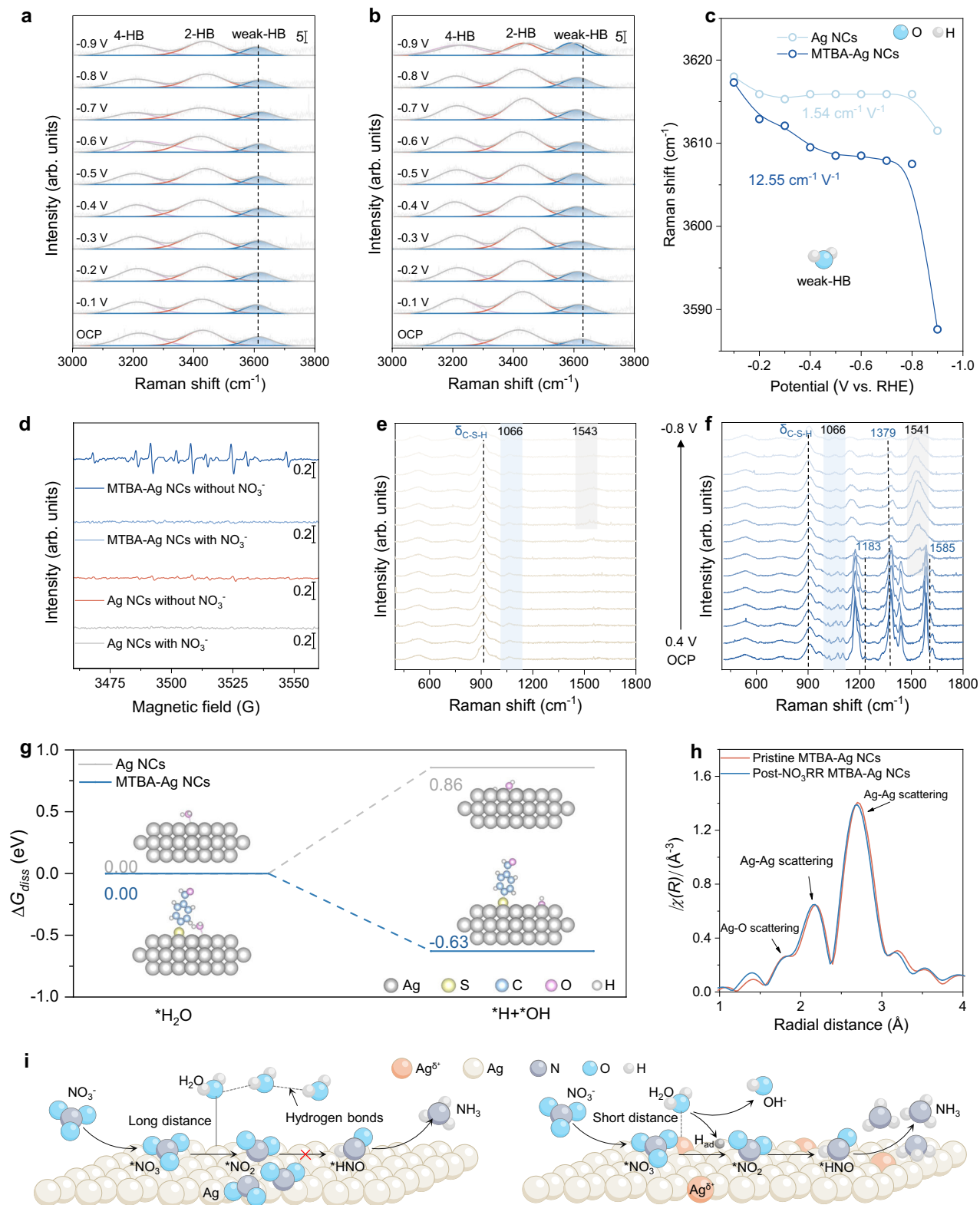


Fig. 4 | Mechanistic investigation of Ag NCs and MTBA-Ag NCs during NO₃RR. In situ Raman spectra of interfacial H₂O on **a** Ag NCs and **b** MTBA-Ag NCs. **c** Potential-dependent Raman shift of weakly hydrogen-bonded H₂O. **d** Quasi in situ EPR detection of hydrogen radicals. In situ Raman spectra of NO₃⁻ reduction

intermediates on **e** Ag NCs and **f** MTBA-Ag NCs. **g** Reaction free-energy diagram for interfacial H₂O dissociation. **h** Fourier-transformed Ag K-edge EXAFS spectra of MTBA-Ag NCs before and after NO₃RR. **i** Proposed NO₃RR pathways on Ag NCs and MTBA-Ag NCs.

fourfold higher than that of Ag NCs/CP device (-50 mA cm^{-2}) (Fig. 5a and Supplementary Fig. 42). Systematic variation of the catholyte flow rate revealed a volcano-type dependence of the NH₃ yield rate, with 3 mL min^{-1} affording the highest rate and FE (Fig. 5b and

Supplementary Fig. 43). At low flow, NO₃⁻ depletion within the porous catalyst layer limits activity, whereas at high flow the shortened residence time curtails per-pass conversion, evidencing through-plane mass-transport control in the MEA⁵². Over a wide current density

range, the optimized MEA delivered a high NH_3 FE of $96 \pm 3\%$ and a yield rate of $7599 \pm 216 \mu\text{g h}^{-1} \text{cm}_{\text{geo}}^{-2}$ at 100 mA cm^{-2} (Fig. 5c and Supplementary Fig. 44). Under extended galvanostatic operation at $100 \text{ mA cm}_{\text{geo}}^{-2}$, the device maintained an average NH_3 FE of 93%, a yield rate of approximately $7400 \mu\text{g h}^{-1} \text{cm}_{\text{geo}}^{-2}$, and a stable cell voltage of 2.1 V for over 108 h without appreciable degradation (Fig. 5d). NH_3 collected via an acid trap was converted to NH_4Cl (Supplementary Figs. 45–47)⁵³, whose identity was confirmed by XRD (Fig. 5e) and by elemental mapping in Supplementary Fig. 48, validating the high purity of the product.

The TEA provides a preliminary assessment of NO_3RR -derived NH_3 production (Fig. 5f–h). The levelized cost was estimated at $-\text{US } \$2.01$ per kg NH_3 , with electricity consumption (40.8%), electrolyzer capital (26.1%), and balance-of-plant (14.0%) identified as the principal cost drivers. Additional contributions arise from maintenance, air stripping, and chemical inputs (KOH and water). Accounting for the potential revenue from NO_3^- wastewater treatment further improves the economic outlook, shifting the net balance towards profitability (Fig. 5f and Supplementary Note 2)⁵⁴. A Sankey diagram (Fig. 5g) breaks down the levelized cost into capital, materials, and operating contributions. Capital expenditure is mainly associated with the electrolyzer stack and balance of plant (together $\approx 40\%$ of the total), while on the operating side electricity alone accounts for $\approx 41\%$, far exceeding maintenance, air stripping, catalyst, KOH, and water, each of which contributes only a few per cent. This cost structure underscores that improvements in energy efficiency and access to low-cost electricity will have a much larger impact on overall economics than further reductions in catalyst or electrolyte consumption. Sensitivity analysis (Fig. 5h) indicates that, at electricity prices below $\text{US}\$0.04 \text{ kWh}^{-1}$, the production cost could fall below the current Haber–Bosch benchmark ($\text{US}\$1.15$ per kg NH_3) at current densities up to 270 mA cm^{-2} ⁵⁵. These results underscore the potential of MTBA–Ag NCs for cost-effective electrosynthesis of NH_3 from NO_3^- -rich waste streams, offering both environmental and economic benefits.

Discussion

In summary, we report a molecular interface engineering strategy to steer NO_3^- electroreduction to NH_3 by anchoring aryl sulfur ligands on Ag NCs. Among the series, MTBA was the most effective modifier, delivering a NH_3 FE of 98.9% and a high yield rate of $14,366.1 \mu\text{g h}^{-1} \text{cm}_{\text{geo}}^{-2}$ at -0.63 V vs. RHE . Spectroscopic analyses combined with theory reveal that MTBA modulates the electronic structure of Ag, facilitating interfacial H_2O activation and accelerating the hydrogenation of $^*\text{NO}_2$ and $^*\text{HNO}$ intermediates, while mitigating competing nitrite pathways. Importantly, MEA measurements confirm that MTBA–Ag NCs sustain high efficiency under device-relevant conditions, and TEA underscores the potential for cost-competitive NH_3 production from NO_3^- -rich wastewater at electricity prices below $\text{US}\$0.04 \text{ kWh}^{-1}$. Beyond identifying a highly selective Ag-based catalyst, this work highlights molecular interface engineering as an effective strategy for the rational design of electrocatalysts for sustainable NH_3 electrosynthesis.

Methods

Synthesis and purification of Ag NCs

Ag NCs were synthesized via a modified polyol method²⁹. Two precursor solutions were prepared: solution A contained silver nitrate (0.50 g) and copper(II) chloride (0.86 μg) in 1,5-pentanediol (12.5 mL), while solution B contained poly(vinyl pyrrolidone) (0.25 g) in 1,5-pentanediol (12.5 mL). 1,5-pentanediol (12.5 mL) was preheated to 190°C in a 100 mL round-bottom flask placed in a silicone oil bath. Solutions A and B were then co-injected at rates of $500 \mu\text{L min}^{-1}$ and $250 \mu\text{L per } 30 \text{ s}$, respectively, until the reaction mixture turned reddish-brown. The mixture was cooled to room temperature ($25 \pm 2^\circ\text{C}$). The Ag NCs were purified by repeated centrifugation at $9500 \times g$ and redispersion

in ethanol, and the final product was stored in ethanol at 4°C for further use.

Surface functionalization of Ag NCs with aryl sulfur ligands

Ag NC suspensions were adjusted to 4 mg mL^{-1} in ethanol and sonicated, then functionalized with aryl sulfur ligands (MBT, ATP, MP, and MBA). A 1 mL aliquot of the suspension was transferred into a 20 mL glass vial with a magnetic stir bar, followed by 1 mL ethanol and 2 mL isopropanol. The mixture was stirred at 500 rpm for 5 min, then $15 \mu\text{L}$ of a 10 mM ethanolic ligand solution was added. The mixture was pipetted five times, sealed, protected from light with aluminum foil, and stirred for 3 h at room temperature ($25 \pm 2^\circ\text{C}$). The product was centrifuged at 10,000 rpm for 4 min, washed three times with ethanol/isopropanol (1:1, v/v), redispersed in 1 mL of the same solvent, and sonicated. Samples not used immediately were sealed with Parafilm and stored at 4°C . For functionalization with MTBA, $10 \mu\text{L}$ neat MTBA was added to 4 mL of a 1 mg mL^{-1} Ag NCs suspension in ethanol. Because MTBA is a neutral aryl thioether rather than a free thiol, its interaction with Ag is weaker and its adsorption kinetics are slower than those of thiolate ligands^{29,30}. To ensure adequate surface functionalization, the suspension was thoroughly sonicated and then stirred at room temperature ($25 \pm 2^\circ\text{C}$) for 6 h, with an additional sonication step after 3 h to maintain dispersion.

Materials characterizations

The crystal structure of the samples was analyzed using XRD (Bruker D2 Phaser). Sample morphology was characterized by SEM (JEOL JSM-7600F microscope). TEM, HRTEM, and the related elemental mapping were conducted on a JEOL JEM-2100 Plus microscope. The electronic states of materials were examined by XPS using a Shimadzu Kratos Axis Supra instrument. UV-Vis absorption spectra were collected on a Shimadzu UV-2700 spectrophotometer. ^1H NMR signals for isotope-labeling experiments were recorded on a Bruker 400 MHz system. XAS, including XANES and EXAFS, was conducted at the Medium Energy X-ray Absorption Spectroscopy Beamline of the Australian Synchrotron. The data were processed using the ATHENA module of the Demeter software package.

Electrochemical measurements (H-cell)

Prior to testing, the Nafion 117 (Suzhou Siner Technology Co., Ltd, $3 \times 3 \text{ cm}^2$, $183\text{-}\mu\text{m}$ thick) was protonated via sequential treatments: (i) immersion in 5% H_2O_2 at 80°C for 2 h, (ii) treatment in 0.5 M sulfuric acid at 80°C for 2 h, and (iii) boiling in deionized (DI) water for 1 h. Glassy carbon electrodes (GCE, 5.0 mm diameter, geometric area 0.196 cm^2) and carbon paper (Fuel Cell Store, $0.5 \times 0.5 \text{ cm}^2$; geometric area 0.25 cm^2) were used as working substrates. GCEs were polished with 50 nm $\alpha\text{-Al}_2\text{O}_3$, rinsed, and sonicated sequentially in isopropanol (IPA) and DI water for 5 min each, then blown dry with Ar. Carbon paper was ultrasonically cleaned in IPA for 10 min and in DI water for 10 min, followed by drying under Ar. To prepare the catalyst ink, $970 \mu\text{L}$ of the Ag NC ethanol dispersion (4.0 mg mL^{-1}) was mixed with $30 \mu\text{L}$ of 5 wt% Nafion D520 dispersion, yielding a total volume of 1.00 mL and a final Ag NC concentration of 3.88 mg mL^{-1} . For GCE, $10 \mu\text{L}$ of the ink was drop-cast onto the polished surface and dried at room temperature ($25 \pm 2^\circ\text{C}$). For carbon paper electrodes, $500 \mu\text{L}$ of the same ink (3.88 mg mL^{-1}) was air-sprayed uniformly onto the pre-cleaned carbon paper in multiple light passes and dried at room temperature ($25 \pm 2^\circ\text{C}$). The electrolyte in both cathode and anode compartments (50 mL each) consisted of 1 M KOH containing 2,000 ppm NO_3^- (pH = 14, measured by an Orion Star A111 pH meter, Thermo Scientific) at room temperature ($25 \pm 2^\circ\text{C}$). High-purity Ar (99.99%) was bubbled into both compartments for at least 30 min prior to each experiment. A Hg/HgO (1 M KOH) reference electrode and a Pt plate counter electrode were used, and all potentials are reported versus the RHE according to $E_{\text{RHE}} = E_{\text{Hg/HgO}} + 0.0591 \times \text{pH} + 0.098 \text{ V}$. All

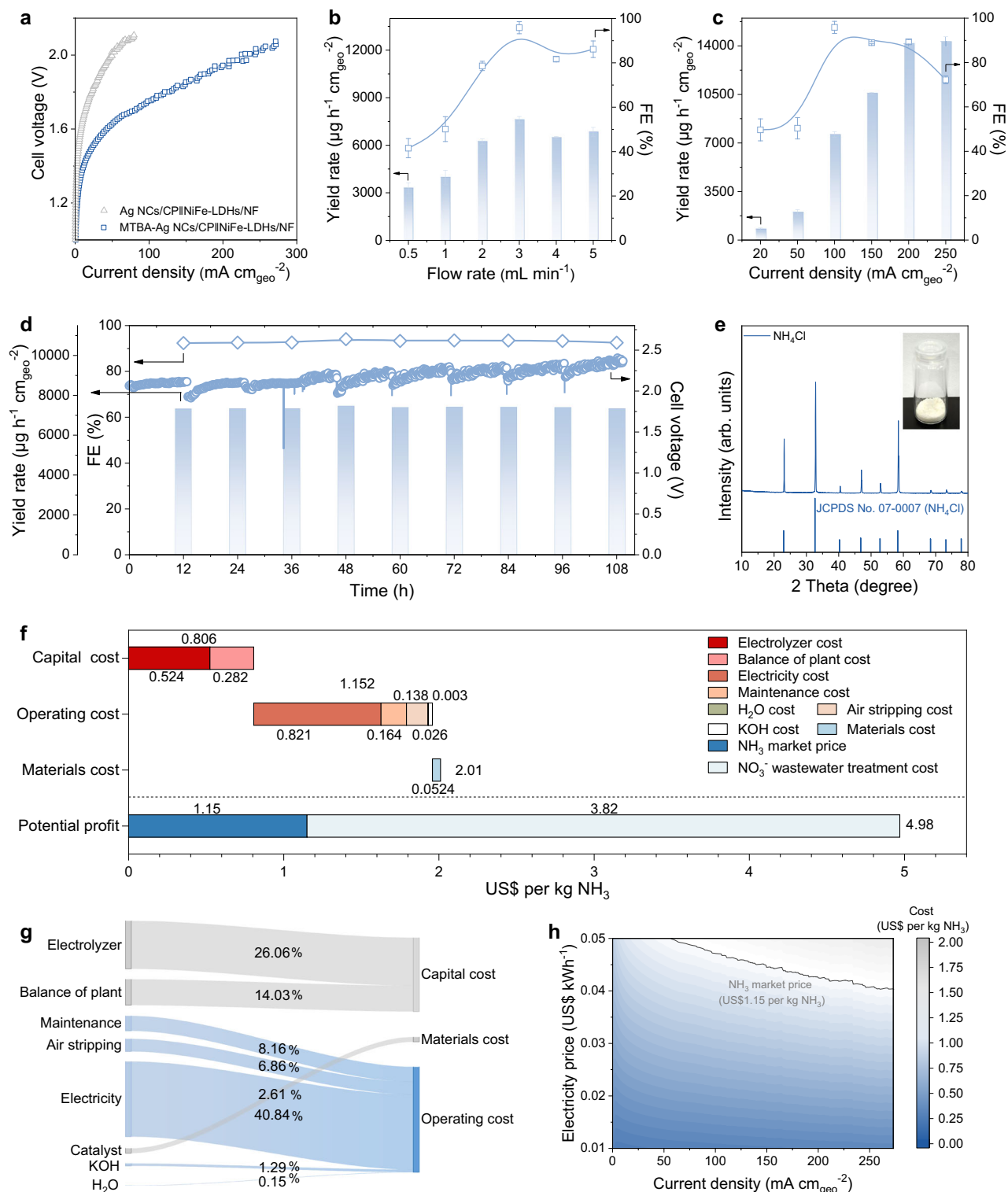


Fig. 5 | Practical NH_3 synthesis and techno-economic analysis. **a** Polarization curves of MEA electrolyzers with Ag NCs/CP and MTBA-Ag NCs/CP cathodes, paired with a NiFe-LDHs/NF anode. **b** NH_3 FEs and yield rates at 100 mA cm^{-2} as a function of electrolyte flow rate. **c** NH_3 FEs and yield rates of MTBA-Ag NCs/CP over a wide current density range. Data represent mean values with standard deviation error bars ($n \geq 3$). **d** Durability test at 100 mA cm^{-2} ,

tracking NH_3 FEs, yield rates, and cell voltage with a MTBA-Ag NCs/CP cathode and a NiFe-LDHs/NF anode. **e** XRD pattern of the collected NH_4Cl product (inset, photograph of NH_4Cl). **f** Breakdown of NH_3 production cost and potential profitability of NO_3RR in the MEA electrolyzer. **g** Sankey diagram of cost contributions. **h** Contour map of NH_3 synthesis cost as a function of current density and electricity price.

electrochemical measurements were performed using a Metrohm AUTOLAB M204 potentiostat. Solution resistance was measured by electrochemical impedance spectroscopy at open circuit, and 50% iR compensation was applied unless otherwise noted.

Chronoamperometry was conducted at fixed potentials for 30 min with magnetic stirring at 900 rpm. Fresh electrolyte, identical Ar purging, and fixed electrode spacing were maintained for all ligand-modified Ag NCs to ensure experimental reproducibility. Cycling

stability was evaluated through 12 repeated potentiostatic electrolysis cycles. Each cycle consisted of 30 min chronoamperometry at -0.63 V versus RHE under identical conditions as described above. Before the start of every cycle, both catholyte and anolyte (1 M KOH containing 2000 ppm NO_3^- , 50 mL each) were purged with Ar for 30 min. Upon completion of each 30-min run, the electrolyte solutions in both compartments were fully replaced with fresh electrolyte to avoid the accumulation of products or intermediates.

ECSA analysis

The electrochemically active surface area was estimated by first determining the double-layer capacitance from CV measurements performed in a potential window free of Faradaic processes. A series of CV scans were collected at different sweep rates (20, 40, 60 to 80 mV s^{-1}), and the capacitive current response at each scan rate was extracted. For each electrode, the difference between anodic and cathodic charging currents was halved and plotted as a function of the scan rate. Linear fitting of these data yielded the double-layer capacitance (C_{dl}). The ECSA was then derived by normalizing C_{dl} with the specific capacitance (C_s), using the relationship:

$$ECSA = C_{dl}/C_s \quad (1)$$

Where C_s represents the specific capacitance of a smooth surface, taken as $40 \mu\text{F cm}^{-2}$ in 1 M KOH⁵⁶.

Ammonia detection

The concentration of NH_4^+ in the catholyte after electrolysis was quantified using the indophenol blue method⁸. Briefly, the catholyte was collected and diluted to fall within the calibration range. Then, 2 mL of the diluted sample was mixed with 2 mL of a 1 M NaOH coloring solution containing 5 wt% salicylic acid and 5 wt% sodium citrate. Subsequently, 1 mL of an oxidizing solution (0.05 M NaClO) and 0.2 mL of a catalyst solution (1 wt% $\text{Na}_2\text{Fe}(\text{CN})_5\text{NO}\cdot 2\text{H}_2\text{O}$) were added to the mixture. The resulting solution was allowed to stand for 2 h in the dark under ambient conditions. Afterward, the absorbance at 655 nm was measured using a UV-Vis spectrophotometer, and the NH_4^+ concentration was determined based on a standard calibration curve prepared using a series of NH_4Cl solutions.

Nitrite detection

The concentration of NO_2^- in the catholyte after electrolysis was quantified using the Griess method⁸. Briefly, a color reagent was prepared by dissolving N-(1-naphthyl)ethylenediamine dihydrochloride (0.1 g) and sulfonamide (1.0 g) in a mixed solution containing H_3PO_4 (2.94 mL) and deionized water (50 mL). The catholyte after electrolysis was diluted tenfold, and 1.0 mL of the diluted sample was mixed with 1.0 mL of the color reagent and 2.0 mL of deionized water. After standing for 10 min under ambient conditions, the absorbance at 540 nm was measured using a UV-Vis spectrophotometer.

Nitrate detection

The concentration of NO_3^- in the catholyte after electrolysis was quantified using UV-Vis spectrophotometry following a standard method⁸. Briefly, an aliquot of the catholyte was collected and diluted to fall within the detection range. Subsequently, 2 mL of the diluted sample was mixed with 100 μL of 1 M HCl and 10 μL of a 0.8 wt% sulfamic acid solution, and the mixture was allowed to stand for 20 min under ambient conditions. The UV-Vis absorption spectrum was then recorded, and the absorbance values at 220 nm and 275 nm were extracted. The corrected absorbance was calculated according to $A = A_{220\text{nm}} - 2A_{275\text{nm}}$. A concentration-absorbance calibration curve was established using a series of standard KNO_3 solutions, with KNO_3 crystals pre-dried at 110°C for 2 h prior to use.

H_2 detection

The gaseous by-product H_2 was monitored and quantified by online gas chromatography (Shimadzu GC-2014C) equipped with a flame ionization detector and a thermal conductivity detector, using Argon gas as the carrier gas. Prior to each experiment, high-purity Argon gas (99.99%) was bubbled through the catholyte for at least 30 min to remove dissolved gases. A Hg/HgO (1 M KOH) electrode and a Pt plate were used as the reference and counter electrodes, respectively.

Calculation of FE, yield rate, and partial current density

The FEs of NO_3RR toward NH_3 and NO_2^- were calculated based on the following equation:

$$FE = \frac{n \times F \times C \times V}{Q} \times 100\% \quad (2)$$

where n is the number of electrons transferred to form the corresponding product, F is the Faraday constant ($96,485 \text{ C mol}^{-1}$), C is the concentration of the product determined experimentally, V is the catholyte volume, and Q is the total charge passed during electrolysis.

The product yield rate was calculated according to:

$$\text{Yield rate} = \frac{C \times V}{M \times t \times A} \quad (3)$$

where M is the molar mass of the product (17 g mol^{-1} for NH_3 and 46 g mol^{-1} for NO_2^-), t is the electrolysis time, and A is the geometric area of the working electrode.

The partial current density for NH_3 was calculated by:

$$i_{\text{NH}_3} = i \times FE_{\text{NH}_3} \quad (4)$$

where i is the total current density applied during electrolysis.

Calculation of EE

EE was calculated using the following equation:

$$EE = (1.23 - E_{\text{NH}_3}) \times FE_{\text{NH}_3} / (1.23 - E) \quad (5)$$

Here, E_{NH_3} (0.69 V) is the equilibrium potential for NO_3^- electroreduction to NH_3 ¹¹, FE_{NH_3} is the FE of NH_3 , 1.23 V is the equilibrium potential of water oxidation (assuming zero overpotential), and E is the potential vs. RHE after 50% iR compensation⁵⁷.

In situ Raman spectroscopy

In situ Raman spectra were collected with a confocal Raman spectrometer (Horiba Jobin Yvon Co., France) using a 633 nm laser. Raman spectra were recorded at different applied potentials with a Metrohm Autolab workstation. A quartz electrochemical cell was positioned beneath the objective lens. Measurements were performed with a confocal Raman microscope equipped with an Olympus 50 \times LDW objective.

Electrochemical online DEMS measurements

The electrolyte (1 M KOH + 2000 ppm NO_3^-) was supplied at 3 mL min^{-1} by a peristaltic pump. A glassy carbon electrode coated with MTBA-Ag NCs was used as the working electrode, with a Pt wire and an Ag/AgCl electrode serving as the counter and reference electrodes, respectively. Potentiostatic polarization at -1.72 V versus Ag/AgCl for 2 min was alternated with 2 min open-circuit intervals to remove residual gas, and the cycle was repeated 10 times after baseline stabilization.

^{15}N isotope-labeling experiment

To qualitatively confirm the source of NH_3 , 1 M KOH containing 2000 ppm K^{15}NO_3 (> 98 atom% ^{15}N) was used as the electrolyte. After $^{15}\text{NO}_3^-$

electroreduction for 30 min, the electrolyte was collected, diluted to the appropriate detection range, and adjusted to pH 2 using 0.1 M HCl. Subsequently, 0.5 mL of the solution was mixed with DMSO- d_6 (hexadeuterodimethyl sulfoxide) containing 0.04 wt% maleic acid for ^1H NMR analysis.

Quasi in situ EPR measurements

EPR spectra were collected to detect radicals or intermediates generated during electrochemical reactions. Chronoamperometry was performed at a constant potential for 5 min, during which radicals or intermediates were trapped by DMPO. The solution was then immediately extracted for subsequent EPR analysis.

Computational details

All calculations were performed using the Vienna Ab initio Simulation Package, within the framework of spin-polarized DFT⁵⁸. Exchange-correlation energies were described using the generalized gradient approximation with the Perdew-Burke-Ernzerhof functional^{59–61}. A plane-wave basis set with a cutoff energy of 600 eV was employed to describe valence electrons, while core electrons were treated with projector augmented wave pseudopotentials⁶². The electronic self-consistency criterion was set to 10^{-5} eV. All the atomic positions and lattice constants were relaxed until the residual forces were smaller than $0.01 \text{ eV } \text{\AA}^{-1}$. Gaussian smearing with a width of 0.05 eV was used for Brillouin-zone integration. For structural optimizations, a Γ -centered $3 \times 3 \times 1$ Monkhorst-Pack k-point mesh was used, whereas a $6 \times 6 \times 1$ mesh was applied for the density of states calculations. The van der Waals interactions were initially excluded owing to strong interfacial bonding. A vacuum layer of 15 \AA was applied to avoid spurious slab-slab interactions. The Ag (100) surface was modeled as a three-layer slab, with the bottom layer fixed and the top two layers relaxed. Dispersion-corrected DFT-D3 was employed to account for van der Waals interactions. Bader charge analysis was performed using the code developed by Henkelman and co-workers⁶³. Solvent and interfacial electrostatic effects were incorporated using an implicit solvation framework implemented in the VASPsol package, where the electrolyte was treated as a dielectric continuum with a relative permittivity of 78.4. The cavitation term was excluded by setting the effective surface tension parameter to zero. Long-range electrolyte screening at the electrode–electrolyte interface was described using a linearized Poisson–Boltzmann approach with a Debye screening length of 3.0 \AA ⁶⁴. All electronic structure calculations were carried out with the “Accurate” precision mode. To simulate electrochemical conditions, a constant-potential scheme was adopted by systematically adjusting the total charge of each slab model from -0.4 e to $+0.4 \text{ e}$ with an increment of 0.1 e . For each charge state, the corresponding potential-dependent energy was evaluated using:

$$E = E_{\text{scf}} + E_{\text{corr}} - q\varphi_q \quad (6)$$

where E_{scf} is the self-consistent DFT energy, q is the net excess charge, and φ_q denotes the work function of the charged surface. The background charge correction term E_{corr} was obtained by integrating the average electrostatic potential of the system, $\langle V_{\text{tot}} \rangle$, with respect to the applied charge:

$$E_{\text{corr}} = \int_0^q \langle \bar{V}_{\text{tot}} \rangle dQ \quad (7)$$

The electrode potential (U_q) relative to the standard hydrogen electrode (SHE) was then determined from the surface work function according to:

$$U_q = -4.6 - \varphi_q / eV \quad (8)$$

where 4.6 V corresponds to the absolute potential of the SHE as implemented in VASPsol. The variation of the system energy with electrode potential was fitted using a quadratic form:

$$E(U_q) = -\frac{1}{2}C(U_q - U_0)^2 + E_0 \quad (9)$$

in which C is the interfacial capacitance, U_0 is the potential of zero charges, and E_0 is the energy at U_0 .

The atomic coordinates of the optimized computational models employed in the Gibbs free energy calculations are provided in Supplementary Data 1. Structural visualizations were generated using the VESTA software.

NO_3^- electrolysis in MEA system

Prior to assembly, the membrane used in the MEA was pre-treated to ensure full ionic conversion. An Alkymer W-25 anion-exchange membrane (AEM) was converted to the OH^- form by soaking in 1 M KOH at 80°C for 24 h, followed by three to four rinses with DI water, and the membrane was kept hydrated until assembly. For MEA cathodes, the catalyst ink was prepared by mixing 0.80 mL IPA, 10 μL of 5 wt% Na^+ -exchanged Nafion, 56.3 μL of MTBA-Ag NC suspension (4.0 mg mL^{-1}), and 1.0 mg carbon black (CB), followed by 1 h ultrasonication to ensure uniform dispersion. The ink was air-sprayed uniformly onto the pre-cleaned carbon paper ($1.5 \times 1.5 \text{ cm}^2$) in multiple light passes and dried at room temperature ($25 \pm 2^\circ\text{C}$), yielding a Ag loading of 0.10 mg cm^{-2} when the entire batch (0.8663 mL) was sprayed. For other ligand-modified Ag NCs, identical ionomer content (Nafion in IPA), CB:Ag ratio, total solids, spray parameters, and drying conditions were maintained to avoid wetting- or transport-related biases, with only the surface ligand on Ag NCs varied. The anode (NiFe-LDH/NF) was prepared via a hydrothermal method⁶⁵. NF ($2 \times 3 \text{ cm}^2$) was ultrasonically cleaned sequentially in 1 M HCl, acetone, and DI water for 10 min each, rinsed thoroughly with DI water, and dried at 60°C for 2 h. A precursor solution was prepared by dissolving 560.1 mg $\text{Ni}(\text{NO}_3)_2 \cdot 6\text{H}_2\text{O}$, 600 mg urea, 111.1 mg $\text{Fe}(\text{NO}_3)_3 \cdot 9\text{H}_2\text{O}$, and 148.2 mg NH_4F in 40 mL DI water under continuous stirring. The solution and a pre-treated NF were transferred into a 50 mL Teflon-lined stainless-steel autoclave and heated at 120°C for 5 h. After naturally cooling to room temperature ($25 \pm 2^\circ\text{C}$), the electrode was removed, rinsed thoroughly with DI water, and dried at 60°C . The custom MEA cell consisted of two titanium current-collector plates, polytetrafluoroethylene gaskets with a 4.0 cm^2 window, and an Alkymer W-25 AEM ($2 \times 2 \text{ cm}^2$) sandwiched between the electrodes. The stack was assembled with 6 N·m torque per bolt. During operation, a 1 M KOH solution containing 2000 ppm NO_3^- was circulated through the cathode side, while another 1 M KOH solution was circulated on the anode side. A fully sealed recirculation system was employed to prevent NH_3 volatilization.

Collection and isolation of NH_4Cl product

Following NO_3RR tests conducted at a current density of 100 mA cm^{-2} , 200 mL of the cathodic electrolyte was transferred to a conical flask. Argon gas was continuously bubbled through the solution while maintaining the temperature at 70°C for 12 h to strip dissolved NH_3 . The volatilized NH_3 was subsequently captured in 200 mL of a 0.3 M HCl solution. The resulting NH_4Cl -containing solution was concentrated by rotary evaporation at 70°C for 3 h and then dried overnight in an oven.

Data availability

The data that support the findings of this study are available within the paper and supplementary information. Additional datasets are available from the corresponding author on request. Source data are provided with this paper.

References

- Christensen, C. H. et al. Towards an ammonia-mediated hydrogen economy? *Catal. Today* **111**, 140–144 (2006).
- Chen, J. G. et al. Beyond fossil fuel-driven nitrogen transformations. *Science* **360**, eaar6611 (2018).
- Nielsen, A. *Ammonia: Catalysis and Manufacture* (Springer, 1995).
- Zhang, L. et al. High-performance electrochemical NO reduction into NH₃ by MoS₂ nanosheet. *Angew. Chem. Int. Ed.* **60**, 25263–25268 (2021).
- International Fertilizer Association. *IFA Short-Term Fertilizer Outlook 2024*. https://www.fertilizer.org/wp-content/uploads/2025/02/2024_ifa_short_term_outlook_report.pdf (2024).
- Erismann, J. W. et al. How a century of ammonia synthesis changed the world. *Nat. Geosci.* **1**, 636–639 (2008).
- Wang, Y. et al. Nitrate electroreduction: mechanism insight, in situ characterization, performance evaluation, and challenges. *Chem. Soc. Rev.* **50**, 6720–6733 (2021).
- Zhang, L. et al. High-efficiency ammonia electrosynthesis from nitrate on ruthenium-induced trivalent cobalt sites. *Energy Environ. Sci.* **18**, 5622–5631 (2025).
- Chen, G.-F. et al. Electrochemical reduction of nitrate to ammonia via direct eight-electron transfer using a copper-molecular solid catalyst. *Nat. Energy* **5**, 605–613 (2020).
- Sun, S. et al. Spin-related Cu-Co pair to increase electrochemical ammonia generation on high-entropy oxides. *Nat. Commun.* **15**, 260 (2024).
- Chen, F. et al. Efficient conversion of low-concentration nitrate sources into ammonia on a Ru-dispersed Cu nanowire electrocatalyst. *Nat. Nanotechnol.* **17**, 759–767 (2022).
- Wu, Q. et al. Efficient electrocatalytic nitrate-to-ammonia enabled by reversible lattice-oxygen control. *J. Am. Chem. Soc.* **147**, 30401–30411 (2025).
- Van, P. H. et al. Electrocatalytic nitrate reduction for sustainable ammonia production. *Joule* **5**, 290–294 (2021).
- Liang, J. et al. Advances in ammonia electrosynthesis from ambient nitrate/nitrite reduction. *Chem* **9**, 1768–1827 (2023).
- Han, S. et al. Ultralow overpotential nitrate reduction to ammonia via a three-step relay mechanism. *Nat. Catal.* **6**, 402–414 (2023).
- Liu, D. et al. Recent advances in electrocatalysts for efficient nitrate reduction to ammonia. *Adv. Funct. Mater.* **33**, 2303480 (2023).
- Liu, H. et al. Electrocatalytic nitrate reduction on oxide-derived silver with tunable selectivity to nitrite and ammonia. *ACS Catal.* **11**, 8431–8442 (2021).
- Yang, H. et al. Pyridine functionalized silver nanosheets for nitrate electroreduction. *J. Mater. Chem. A* **11**, 16068–16073 (2023).
- Zhang, R. et al. Molecular engineering of a metal-organic polymer for enhanced electrochemical nitrate-to-ammonia conversion and zinc nitrate batteries. *Angew. Chem. Int. Ed.* **62**, e202309930 (2023).
- Deng, Y. et al. Mechanical and covalent tailoring of copper catenanes for selective aqueous nitrate-to-ammonia electrocatalysis. *J. Am. Chem. Soc.* **147**, 14316–14325 (2025).
- Lee, Y. et al. Nanoscale surface chemistry directs the tunable assembly of silver octahedra into three two-dimensional plasmonic superlattices. *Nat. Commun.* **6**, 6990 (2015).
- Ren, Z. et al. Complete single-pass conversion of dilute nitrate to ammonia using Cu/Co(OH)₂ tandem electrocatalyst. *ACS Energy Lett.* **9**, 3849–3858 (2024).
- Matsubara, Y. et al. Thermodynamic aspects of electrocatalytic CO₂ reduction in acetonitrile and with an ionic liquid as solvent or electrolyte. *ACS Catal.* **5**, 6440–6452 (2015).
- Yu, D. et al. Controlled synthesis of monodisperse silver nanocubes in water. *J. Am. Chem. Soc.* **126**, 13200–13201 (2004).
- Hansch, C. et al. A survey of Hammett substituent constants and resonance and field parameters. *Chem. Rev.* **91**, 165–195 (1991).
- Bai, L. et al. Electrocatalytic nitrate and nitrite reduction toward ammonia using Cu₂O nanocubes: active species and reaction mechanisms. *J. Am. Chem. Soc.* **146**, 9665–9678 (2024).
- Gao, Q. et al. Breaking adsorption-energy scaling limitations of electrocatalytic nitrate reduction on intermetallic CuPd nanocubes by machine-learned insights. *Nat. Commun.* **13**, 2338 (2022).
- Wu, Z. et al. Electrochemical ammonia synthesis via nitrate reduction on Fe single atom catalyst. *Nat. Commun.* **12**, 2870 (2021).
- Tao, A. et al. Polyhedral silver nanocrystals with distinct scattering signatures. *Angew. Chem. Int. Ed.* **45**, 4597–4601 (2006).
- Tan, E. X. et al. Forward-predictive SERS-based chemical taxonomy for untargeted structural elucidation of epimeric cerebrosides. *Nat. Commun.* **15**, 2582 (2024).
- Kaspar, T. C. et al. Spectroscopic evidence for Ag(III) in highly oxidized silver films by X-ray photoelectron spectroscopy. *J. Phys. Chem. C* **114**, 21562–21571 (2010).
- Liu, Y. et al. Silver nanoparticle enhanced metal-organic matrix with interface-engineering for efficient photocatalytic hydrogen evolution. *Nat. Commun.* **14**, 541 (2023).
- Kao, J. et al. Single atom Ag bonding between PF₃T nanocluster and TiO₂ leads the ultra-stable visible-light-driven photocatalytic H₂ production. *Small* **20**, 2403176 (2024).
- Jiang, X. et al. Silver single atom in carbon nitride catalyst for highly efficient photocatalytic hydrogen evolution. *Angew. Chem. Int. Ed.* **59**, 23112–23116 (2020).
- Liu, J. et al. Understanding Au₉₈Ag₄₆(SR)₆₀ nanoclusters through investigation of their electronic and local structure by X-ray absorption fine structure. *RSC Adv.* **6**, 25368–25374 (2016).
- Padmos, J. D. et al. Impact of protecting ligands on surface structure and antibacterial activity of silver nanoparticles. *Langmuir* **31**, 3745–3752 (2015).
- Hu, S. et al. Selective photocatalytic reduction of CO₂ to CO mediated by silver single atoms anchored on tubular carbon nitride. *Angew. Chem. Int. Ed.* **62**, e202304585 (2023).
- Yang, H. et al. Manganese vacancy-confined single-atom Ag in cryptomelane nanorods for efficient Wacker oxidation of styrene derivatives. *Chem. Sci.* **12**, 6099–6106 (2021).
- Li, J. et al. Capture of single Ag atoms through high-temperature-induced crystal plane reconstruction. *Nat. Commun.* **15**, 3874 (2024).
- Fernández-Nava, Y. et al. Denitrification of wastewater containing high nitrate and calcium concentrations. *Bioresour. Technol.* **99**, 7976–7981 (2008).
- Wang, Y. H. et al. In situ Raman spectroscopy reveals the structure and dissociation of interfacial water. *Nature* **600**, 81–85 (2021).
- Zhang, T. et al. Positively charged hollow Co nanoshells by Kirkendall effect stabilized by electron sink for alkaline water dissociation. *Adv. Mater.* **36**, 2405386 (2024).
- Zhou, R. et al. Elevating nitrate reduction through the mastery of hierarchical hydrogen-bond networks. *J. Am. Chem. Soc.* **147**, 20504–20511 (2025).
- Weatherston, J. D. et al. Quantitative surface-enhanced Raman spectroscopy for kinetic analysis of aldol condensation using Ag-Au core-shell nanocubes. *Analyst* **141**, 6051–6060 (2016).
- Lei, F. et al. Electrochemical reduction of nitrate on silver surface and an in situ Raman spectroscopy study. *Inorg. Chem. Front.* **9**, 2734–2740 (2022).
- Wu, D. et al. Electrochemical surface-enhanced Raman spectroscopy of nanostructures. *Chem. Soc. Rev.* **37**, 1025–1041 (2008).
- Xu, M. et al. Aqueous divalent metal-nitrate interactions: hydration versus ion pairing. *Phys. Chem. Chem. Phys.* **10**, 4793–4801 (2008).
- Ling, Y. et al. NMR, IR/Raman, and structural properties in HNO and RNO (R = Alkyl and Aryl) metalloporphyrins with implication for the HNO-myoglobin complex. *J. Am. Chem. Soc.* **132**, 1583–1591 (2010).

49. Wang, J. et al. In situ X-ray spectroscopies beyond conventional X-ray absorption spectroscopy on deciphering dynamic configuration of electrocatalysts. *Nat. Commun.* **14**, 6576 (2023).
50. Timoshenko, J. & Roldan, B. In situ/operando electrocatalyst characterization by X-ray absorption spectroscopy. *Chem. Rev.* **121**, 882–961 (2021).
51. Clabaut, P. et al. Water adlayers on noble metal surfaces: Insights from energy decomposition analysis. *J. Chem. Phys.* **153**, 054703 (2020).
52. Guo, J. et al. Mass transport modifies the interfacial electrolyte to influence electrochemical nitrate reduction. *ACS Sustain. Chem. Eng.* **11**, 7882–7893 (2023).
53. Yuan, M.-H. et al. Ammonia removal from ammonia-rich wastewater by air stripping using a rotating packed bed. *Process Saf. Environ. Prot.* **102**, 777–785 (2016).
54. U.S. Energy Information Administration (EIA). Levelized cost and levelized avoided cost of new generation resources. https://www.eia.gov/outlooks/aeo/pdf/electricity_generation.pdf (2020).
55. Schnitkey, G. et al. Fertilizer prices and company profits going into spring 2023. *Farmdoc Daily* <https://farmdocdaily.illinois.edu/2023/02/fertilizer-prices-and-company-profits-going-into-spring-2023.html> (2023).
56. Jiang, Q. et al. Active oxygen species mediate the iron-promoting electrocatalysis of oxygen evolution reaction on metal oxyhydroxides. *Nat. Commun.* **14**, 6826 (2023).
57. Huang, Y. et al. Pulsed electroreduction of low-concentration nitrate to ammonia. *Nat. Commun.* **14**, 7368 (2023).
58. Burke, K. Perspective on density functional theory. *J. Chem. Phys.* **136**, 150901 (2012).
59. Perdew, J. P. et al. Generalized gradient approximation made simple. *Phys. Rev. Lett.* **77**, 3865–3868 (1996).
60. Kohn, W. et al. Self-consistent equations including exchange and correlation effects. *Phys. Rev.* **140**, A1133–A1138 (1965).
61. Perdew, J. P. et al. Atoms, molecules, solids, and surfaces: applications of the generalized gradient approximation for exchange and correlation. *Phys. Rev. B* **46**, 6671–6687 (1992).
62. Kresse, G. et al. From ultrasoft pseudopotentials to the projector augmented-wave method. *Phys. Rev. B* **59**, 1758–1775 (1999).
63. Henkelman, G. et al. A fast and robust algorithm for Bader decomposition of charge density. *Comput. Mater. Sci.* **36**, 354–360 (2006).
64. Wu, Q. et al. Potential and electric double-layer effect in electrocatalytic urea synthesis. *Nat. Commun.* **15**, 1095 (2024).
65. Zhang, L. et al. Benzoate anions-intercalated NiFe-layered double hydroxide nanosheet array with enhanced stability for electrochemical seawater oxidation. *Nano Res. Energy* **1**, 9120028 (2022).

Acknowledgements

This work was supported by the National Research Foundation, Prime Minister's Office, Singapore under its Campus for Research Excellence and Technological Enterprise (CREATE) program (Development of advanced catalysts for electrochemical carbon abatement), Project Code: 370184872, National Natural Science Foundation of China (22425804), Natural Science Foundation of Sichuan Province (2025ZNSFSC0899, 2025ZNSFSC0923), and Postdoctoral Joint Training

Program of Sichuan University (SCDXLHPY2303, SCDXLHPY2304). The authors thank Dr. Feng Yang (the Comprehensive Training Platform of the Specialized Laboratory, College of Chemistry, Sichuan University) for her assistance with TEM characterization and Prof. Li Wu (Analytical & Testing Center, Sichuan University) for her help with in situ Raman spectroscopy.

Author contributions

L.Z., X.G., and Z.J.X. conceived the original concept and initiated the project. L.Z. prepared the catalyst materials and wrote the manuscript. Y.L. carried out the theoretical calculations. L.L. performed SEM and in situ Raman measurements. L.Z. conducted the remaining characterizations with assistance from X.L. (XAS), P.S. (HADD-STEM), J.Z.Y.S. (XRD), K.T. (XPS), and S.S. (NMR). T.C. and Q.W. performed the data analysis. All authors discussed the results and contributed to the manuscript.

Competing interests

The authors declare no competing interests.

Additional information

Supplementary information The online version contains supplementary material available at <https://doi.org/10.1038/s41467-026-69385-1>.

Correspondence and requests for materials should be addressed to Xiaodong Guo or Zhichuan J. Xu.

Peer review information *Nature Communications* thanks Lihui Ou and the other anonymous reviewer(s) for their contribution to the peer review of this work. A peer review file is available.

Reprints and permissions information is available at <http://www.nature.com/reprints>

Publisher's note Springer Nature remains neutral with regard to jurisdictional claims in published maps and institutional affiliations.

Open Access This article is licensed under a Creative Commons Attribution-NonCommercial-NoDerivatives 4.0 International License, which permits any non-commercial use, sharing, distribution and reproduction in any medium or format, as long as you give appropriate credit to the original author(s) and the source, provide a link to the Creative Commons licence, and indicate if you modified the licensed material. You do not have permission under this licence to share adapted material derived from this article or parts of it. The images or other third party material in this article are included in the article's Creative Commons licence, unless indicated otherwise in a credit line to the material. If material is not included in the article's Creative Commons licence and your intended use is not permitted by statutory regulation or exceeds the permitted use, you will need to obtain permission directly from the copyright holder. To view a copy of this licence, visit <http://creativecommons.org/licenses/by-nc-nd/4.0/>.

© The Author(s) 2026